THE ASTROPHYSICAL JOURNAL, 517:609–621, 1999 June 1
© 1999. The American Astronomical Society. All rights reserved. Printed in U.S.A.

MEASURABILITY OF KINETIC TEMPERATURE FROM METAL ABSORPTION-LINE SPECTRA FORMED IN CHAOTIC MEDIA[1]

SERGEI A. LEVSHAKOV
National Astronomical Observatory, Mitaka, Tokyo 181, Japan
FUMIO TAKAHARA
Department of Earth and Space Science, Faculty of Science, Osaka University, Toyonaka, Osaka 560, Japan
AND
IRINA I. AGAFONOVA
National Astronomical Observatory, Mitaka, Tokyo 181, Japan
Received 1998 September 11; accepted 1999 January 16

ABSTRACT

We present a new method for recovering the kinetic temperature of the intervening diffuse gas to an accuracy of 10%. The method is based on the comparison of unsaturated absorption-line profiles of two species with different atomic weights. The species are assumed to have the same temperature and bulk motion within the absorbing region. The computational technique involves the Fourier transform of the absorption profiles and the consequent entropy-regularized χ^2-minimization (ERM) to estimate the model parameters. The procedure is tested using synthetic spectra of C^+, Si^+, and Fe^+ ions. The comparison with the standard Voigt fitting analysis is performed, and it is shown that the Voigt deconvolution of the complex absorption-line profiles may result in estimated temperatures that are not physical. We also successfully analyze Keck telescope spectra of C II λ1334 and Si II λ1260 lines observed at the redshift $z = 3.572$ toward the quasar Q1937−1009 by Tytler et al.

Subject headings: quasars: absorption lines — quasars: individual (1937−1009) — radiative transfer — ultraviolet: galaxies

1. INTRODUCTION

The new generation of large telescopes enables us to study the intergalactic and interstellar absorbing gas with instrumental resolutions sufficiently high to resolve absorption features into their individual subcomponents. From absorption-line spectra, one usually estimates the column densities of absorbing species, N, the Doppler b-parameter of the diffuse gas, and the positions (i.e., radial velocities) of the subcomponents that are traditionally considered to be caused by the intervening "clouds."

The observations show the ubiquitous asymmetry of the line profiles (Spitzer & Fitzpatrick 1993; Huang et al. 1995; Lu et al. 1996; Prochaska & Wolfe 1997). Their widths are believed to reflect the sum of thermal and nonthermal ("bulk" or "turbulent") motion. It should be noted that the term "turbulent" as used in spectroscopy is not as distinct as hydrodynamic turbulence and labels the *lack* of information about the nature of the broadening mechanism (Traving 1975). Therefore, in order to treat observations a model of the line broadening is to be specified first of all.

It is a common assumption that both thermal and turbulent velocities along a given line of sight can be represented by Gaussian distributions, i.e., that thermal and nonthermal broadening can be added quadratically:

$$b^2 = v_{\rm th}^2 + 2\sigma_t^2 \ . \tag{1}$$

Here σ_t is the rms turbulent velocity and $v_{\rm th}$ is the thermal velocity,

$$v_{\rm th} = \sqrt{2k_{\rm B}\,T/m_a} \ , \tag{2}$$

where $k_{\rm B}$ is Boltzmann's constant, m_a is the mass of the element, and T is the kinetic temperature.

To separate the contribution of thermal and turbulent motion one usually utilizes the line profiles of different elements assuming that they have the same temperature and velocity distribution within the individual components. If this is the case, then higher mass elements should have lower apparent b-values, provided that the measurements have a sufficiently high spectral resolution. With such reservations one can solve equation (1) for T and σ_t for different species.

Applied to the real absorption-line spectra, this technique often leads, however, to an implausibly wide range of T among individual "cloudlets," yielding for some of them even unphysical negative kinetic temperatures—clearly an absurdity (Spitzer & Fitzpatrick 1993, 1995; Fitzpatrick & Spitzer 1997; Tripp, Lu, & Savage 1997). This suggests that in general the problem of the b-parameter measurement from the interstellar and/or quasar metal absorption-line spectra is *far from being solved.*

To a certain extent this problem is connected with the interpretation of complex absorption features as being caused mainly by density fluctuations. However, as shown by Levshakov & Kegel (1997), the intensity fluctuations within the line profile can occur as a result of correlation effects in the large-scale velocity field even for the homogeneous gas density.

The present paper is primarily aimed at the problem of the kinetic temperature measurement accounting for these correlation effects. The analysis employs absorption profiles of two species with different atomic weights. These profiles are considered to arise in a transparent absorbing region of thickness L with a correlated velocity field and a homogeneous temperature T. Although in principle density fluctuations can be incorporated, here we confine ourselves to the

[1] Based in part on data obtained at the W. M. Keck Observatory, which is jointly operated by the University of California and the California Institute of Technology.

case of the homogeneous gas density and, hence, the density ratio of the chosen elements is constant along the line of sight. These conditions yield the similarity in the observed profiles of different elements (examples can be found in Spitzer & Fitzpatrick 1993 or in Songaila 1998). The assumption of constant T is supported by the fact that the states of thermally stable, optically thin interstellar gas take only limited temperature ranges over a relatively wide range of density variations (see, e.g., Fig. 8.9 in Shu 1992).

The entropy-regularized χ^2-minimization (ERM) method we propose allows a robust measurement of a single value of T from the multicomponent (complex) absorption spectra in cases where the standard Voigt-profile fitting procedure yields different values of T for the different subcomponents. The description of our model and its basic assumptions is given in § 2. A study of the accuracy of the method is provided through a series of numerical simulations of complex spectra produced in the correlated velocity fields of different structure that is presented in § 3. We proceed further in this approach with high-resolution C II λ1334 and Fe II λ2600 synthetic spectra in § 4, in order to derive the gas temperature and to compare its value with the standard Voigt fitting procedure yield. An example based on real observations of high-redshifted metal absorption lines is presented in this section as well. We summarize our conclusions in § 5.

2. DATA ANALYSIS TECHNIQUE

In this section we present a compendium of the standard radiative transfer equations describing pure absorption in spectral lines and the analytical technique to derive the T estimation and the radial velocity distribution function ϕ_t from the line profiles of two elements with different atomic weights. Here we are dealing with noiseless data, assuming that the given spectra are exact.

2.1. *Basic Equations*

If the interstellar (intergalactic) absorption line is optically thin, one observes directly the apparent optical depth $\tau^*(\lambda)$ as function of wavelength λ

$$\tau^*(\lambda) = \ln\ [I_0(\lambda)/I_{\rm obs}(\lambda)]\ , \tag{3}$$

where $I_{\rm obs}(\lambda)$ and $I_0(\lambda)$ are the intensities with and without the absorption, respectively.

The recorded spectrum is a convolution of the true spectrum and the spectrograph point-spread function $\phi_{\rm sp}$

$$I_{\rm obs}(\lambda) = \int_{-\infty}^{+\infty} I_0(\lambda') e^{-\tau(\lambda')} \phi_{\rm sp}(\lambda - \lambda')\, d\lambda'\ , \tag{4}$$

where $\tau(\lambda)$ is the true (intrinsic) optical depth.

The intensity of the background continuum source $I_0(\lambda)$ changes usually very slowly over the width of the spectrograph function, and hence equation (4) becomes

$$I_{\rm obs}(\lambda) = I_0(\lambda) \int_{-\infty}^{+\infty} e^{-\tau(\lambda')} \phi_{\rm sp}(\lambda - \lambda')\, d\lambda'\ . \tag{5}$$

For the following it is convenient to change from λ-space to the radial velocity v-space. Further, let the line-absorption coefficient reckoned per atom (the absorption cross section) at radial velocity v within the line profile be denoted by $k(v)$. Then the optical depth at velocity v is

$$\tau(v) = Nk(v)\ . \tag{6}$$

For the case of unsaturated absorption lines when the effect of radiation damping is negligible, $k(v)$ may be described by the Doppler kernel of the Voigt function (Spitzer 1978). Then the profile function is defined *locally* by the thermal broadening, i.e., the line width is determined by the kinetic temperature only ($b = v_{\rm th}$). Now $k(v)$ can be expressed as the product of a constant k_0 for a particular line and the Gaussian line profile function $\phi_{\rm th}(v)$

$$k(v) \equiv k_0\, \phi_{\rm th}(v) = \frac{\pi e^2}{m_e c} f_{\rm abs}\, \lambda_0\, \frac{1}{\sqrt{\pi} v_{\rm th}}\, e^{-(v - v_0)^2/v_{\rm th}^2}\ , \tag{7}$$

where m_e and e are the mass and charge of the electron and $f_{\rm abs}$ and λ_0 are the oscillator strength and the wavelength of the line center at which the corresponding radial velocity is equal to v_0.

If atoms are involved in both thermal and hydrodynamic motions and the temperature is constant along the line of sight, then the total line profile function is a convolution of $\phi_{\rm th}(v)$ and the radial velocity distribution function $\phi_t(v)$ caused by bulk motion

$$\phi_{\rm tot}(v) = \int_{-\infty}^{+\infty} \phi_t(v') \phi_{\rm th}(v - v')\, dv'\ , \tag{8}$$

and $\tau(v) = Nk_0\, \phi_{\rm tot}(v)$.

Both functions ϕ_t and $\phi_{\rm th}$ are normalized so that $\int (\cdot)\, dv = 1$. In principle, ϕ_t reflects the density fluctuations as well and in reality is the density-weighted radial velocity distribution, but while we are dealing with the similar profiles the explicit treatment of the density fluctuations can be avoided. The instrumental point-spread function $\phi_{\rm sp}$ can be determined experimentally, whereas ϕ_t and $\phi_{\rm th}$ are the two contributions of astrophysical interest.

2.2. *T and $\phi_t(v)$ Calculations*

We now consider how to measure the kinetic temperature T from the complex profiles of a pair of elements with different masses. It is a task to deconvolve the thermal and the turbulent profiles, both of which are unknown a priori. We are mainly interested in cases in which line profiles are dominated by nonthermal broadening, $\sigma_t/v_{\rm th} \gtrsim 1$; otherwise the problem is trivial.

Let us assume that two ions have different masses, m_i, and $m_2 > m_1$. For a fixed value of v within the line profile, the optical depth is given according to equations (6)–(8) by

$$\tau_i(v) = \omega_i \int_{-\infty}^{+\infty} \phi_t^i(v') \phi_{\rm th}^i(v - v')\, dv', \qquad i = 1, 2\ , \tag{9}$$

where $\omega_i = k_0^i N_i$.

This equation is a convolution of two functions. Its Fourier transform is

$$\hat{\tau}_i(q) = \int_{-\infty}^{+\infty} \tau_i(v) e^{2\pi i q v}\, dv = \omega_i\, \hat{\phi}_{\rm th}^i(q) \hat{\phi}_t^i(q), \qquad i = 1, 2\ , \tag{10}$$

where $\hat{\phi}_{\rm th}^i(q)$ and $\hat{\phi}_t^i(q)$ are the Fourier transforms of the line-profile function $\phi_{\rm th}^i(v)$ and the radial velocity distribution function $\phi_t^i(v)$, respectively.

If the chosen ions trace the *same* volume elements and the ionization fraction is *equal* for both of them (this assumption may not be universally true for any pair of ions but is expected to be valid for ions with similar ionization potentials), then $\phi_t^1(v) = \phi_t^2(v)$. In this case two Fourier transforms, $\hat{\tau}_1(q)$ and $\hat{\tau}_2(q)$, yield the *exact* equations rela-

ting the line shapes in the Fourier space to the kinetic temperature *independent* of the velocity and density fluctuations along a given line of sight:

$$\Re\left[\frac{\hat{\tau}_2(q)}{\hat{\tau}_1(q)}\right] = \frac{\omega_2}{\omega_1}\, e^{q^2\pi^2(v_{\mathrm{th},1}^2 - v_{\mathrm{th},2}^2)} \equiv \frac{\omega_2}{\omega_1}\, e^{aTq^2\pi^2}\,,$$

$$\Im\left[\frac{\hat{\tau}_2(q)}{\hat{\tau}_1(q)}\right] = 0\,, \tag{11}$$

where $a = 2k_{\mathrm{B}}(m_2 - m_1)/(m_1 m_2)$ is a numerical constant.

In the calculation of T from equation (11) the first step is to determine the Fourier transforms $\hat{\tau}_1$ and $\hat{\tau}_2$. The most appropriate way would be to represent τ by a set of functions that have an analytical Fourier transform. We have chosen Gaussian functions, since irregular Doppler shifts of the local absorption coefficient (eq. [7]) along the sight line, yielding the apparent complexity of the line profiles, result in a mixture of the Gaussian functions (eq. [8]). The line profiles are modeled using the sum of Gaussian functions:

$$\tau_i(v) = \frac{1}{\sqrt{\pi}\beta_i}\sum_{j=1}^{M} a_{i,j}\, e^{-(v-v_j)^2/\beta_i^2}, \quad i = 1, 2\,. \tag{12}$$

Here M is the number of modes and $a_{1,j}$ and $a_{2,j}$ are their weights. Since the basic assumptions of our method lead to the similarity of both profiles, we may set the number of modes and their centers to be identical, i.e., $M_1 = M_2 = M$ and $v_{1,j} = v_{2,j} = v_j$. All modes describing the individual profile have the same dispersion, denoted β_1 for the first profile and β_2 for the second, with $\beta_2 < \beta_1$. The choice of the equidispersion Gaussian functions is in no way restrictive in our case, because the modes in equation (12) are used only to describe the entire shape of each line profile and do not have any physical meaning. The number of modes M is an arbitrary parameter and is determined solely by a satisfactory fit of τ_1 and τ_2. The equidispersion modes with identical positions make it very easy to meet the second condition in equation (11)—viz., that the imaginary part of the ratio $\hat{\tau}_2/\hat{\tau}_1$ is zero—resulting in the requirement $a_{1,j}/a_{2,j} = \xi =$ constant for all j.

It should be noted that the multi-Gaussian model (eq. [12]) is not the only one that describes the shape of the profiles. Any other representation can be used as well. Nevertheless, this model has been favored because of its clearness and easiness in realization. Similar profiles can be always fitted by using this model; on the contrary, if the fit according to equation (12) fails, then the profiles are nonsimilar and hence our method cannot be applied.

Equation (12) shows that the total number of free parameters to be found is equal to $2M + 3$ and that ω can be calculated as

$$\omega_i = \sum_{j=1}^{M} a_{i,j}, \qquad i = 1, 2\,, \tag{13}$$

with $\omega_2/\omega_1 = 1/\xi$.

Using equation (12), the Fourier transforms of the line profiles can be expressed as

$$\hat{\tau}_i(q) = e^{-\pi^2\beta_i^2 q^2}\sum_{j=1}^{M} a_{j,i}\, e^{2\pi i v_j q}, \qquad i = 1, 2\,. \tag{14}$$

From equations (11)–(14) it follows that the kinetic temperature is determined by

$$T = (\beta_1^2 - \beta_2^2)/a\,. \tag{15}$$

Having estimated the kinetic temperature, the radial velocity distribution function $\phi_t(v)$ can be calculated through the inverse Fourier transform

$$\phi_t(v) = \int_{-\infty}^{\infty} \hat{\phi}_t(q) e^{-2\pi i v q}\, dq \tag{16}$$

of the function

$$\hat{\phi}_t(q) = \frac{\hat{\tau}_i(q)}{\omega_i\, \hat{\phi}_{\mathrm{th}}^i(q)}\,, \qquad i = 1, 2\,. \tag{17}$$

From equations (14), (16), and (17) we can readily show that

$$\phi_t(v) = \frac{1}{\omega_i\sqrt{\pi(\beta_i^2 - v_{\mathrm{th},i}^2)}}\sum_{j=1}^{M} a_{i,j}\exp\left[-\frac{(v-v_j)^2}{\beta_i^2 - v_{\mathrm{th},i}^2}\right], \quad i = 1 \text{ or } 2\,. \tag{18}$$

Although in our model β_1 and β_2 are arbitrary parameters without any physical meaning, their natural lower limits should not be smaller than the corresponding thermal widths; otherwise one may be trapped into the fitting of noise. Then it follows that the ratio $\zeta \equiv \beta_2/\beta_1$ ranges between $(m_1/m_2)^{1/2}$ and 1, yielding $\beta_i^2 - v_{\mathrm{th},i}^2 > 0$ for any parameter sets.

3. PRACTICAL IMPLEMENTATION

In the foregoing section we formulated a method to derive the kinetic temperature by using the Fourier transform technique. We have so far dealt with noiseless data. Now we turn our attention to the case of noisy data.

To calculate T from equation (15) we need first of all to estimate $2M + 3$ parameters of model defined by equation (12): β_1, ζ, ξ, v_j, $a_{1,j}$, where $j = 1, \ldots, M$. Since we are primarily interested in the recovery of T, another set of the parameters appears to be more convenient: $\theta = \{T, \zeta, \xi, v_j, a_{1,j}\} \equiv \{\theta_1, \ldots, \theta_{2M+3}\}$, with θ standing for a parameter vector. The standard χ^2 minimization is used to estimate θ:

$$\chi^2(\theta) = \frac{1}{\nu}\sum_{i=1}^{M'}\left[\frac{I(\lambda_i) - I^*(\lambda_i, \theta)}{\Delta I_i}\right]^2, \tag{19}$$

where $I(\lambda_i)$ is the simulated (or observed) normalized intensity within the ith pixel of the line profile and $I^*(\lambda_i, \theta) \equiv \exp\{-\tau(\lambda_i, \theta)\}$ is the calculated intensity. Both are convolved with the instrumental function ϕ_{sp}. Further, ΔI_i is a simulated (or experimental) error, M' is the number of pixels involved in the sum, and $\nu = M' - 2M - 3$ is the number of degrees of freedom. As already mentioned, the choice of the number of modes M is somewhat arbitrary but the minimum number of M is determined by the appropriate quality of the fit ($\chi^2 \lesssim 1$).

Model calculations with different synthetic spectra have shown, however, that the minimization according to equation (19) does not allow us to recover the kinetic temperature with a sufficiently high accuracy (say 10%). The deviations of the recovered temperature from its underlying value exceeded in some cases 100%. This failure is easy to understand: our model for I^* is constructed using several smoothing operators (convolution with the instrumental function and summing in eq. [12]), and, as a result, we have here a typical *ill-posed* problem (see, e.g., Tikhonov & Arsenin 1977). Parameters in ill-posed problems are known to be very sensitive to data perturbations, which results in the inappropriate large dispersions. The ill-posed problems often occur in the astronomical image reconstructions as

well, and several methods have been developed to overcome this obstacle (see Wu 1997 and references cited therein). In order to stabilize the estimation of θ, we need to augment χ^2 by a regularization term penalizing large values of parameter errors. This technique is applied to our particular problem below.

3.1. *The Entropy-regularized χ^2-Minimization Procedure*

This section concerns the entropy-regularized χ^2-minimization (ERM) procedure developed to estimate the best-fit value for the parameter vector θ. To begin with, we formulate the ERM method. Then we state the problem in mathematical language. Finally, we discuss some practical implementations.

Instead of minimizing χ^2, defined in equation (19), we now seek the minimum of another objective function,

$$\mathscr{L}_\alpha(\theta) = \chi^2(\theta) + \alpha\, \psi(\theta)\,, \tag{20}$$

where ψ is a penalty function and α the regularization parameter that is to be estimated. By minimizing equation (20), we find the most probable value of the parameter vector θ_0.

The choice of ψ, especially for nonlinear problems, occurs rather heuristically. Since our purpose is to obtain the most accurate estimation of T, it is reasonable to make ψ penalize large error in temperature. Having $aT = \beta_1^2\ (1 - \zeta^2)$ and $\Delta T/T \propto 1/\beta_1\ (1 - \zeta^2)$, the easiest choice will be

$$\psi = \frac{1}{\beta_1(1 - \zeta^2)}\,, \tag{21}$$

which means that α is in units of velocity.

In spite of its simplicity, this function works quite effectively and enables us to locate the true value of temperature very closely. (It should be noted that when we change the parameter set and make T be a free variable, the form of the regularization term remains the same but with $\beta_1 = [aT/(1 - \zeta^2)]^{1/2}$. This corresponds to the minimization of the relative error in β_1.)

The determination of the optimal value of α is the most crucial point in all regularization procedures. It still remains an open question for linear problems, although the method of Lagrange multipliers, Bayesian estimations, and maximum entropy (MaxEnt) concept has proved to be very successful in many cases. The optimality criterion applied for our problem is motivated by the idea of minimization of the cross entropy, which is in principle equivalent to the MaxEnt approach (Wu 1997). In detail, our procedure is described as follows.

Since entropy is a probabilistic measure of the uncertainty of the information obtained, we will consider the parameter vector θ as a random variable with the probability density function (PDF) $p_\alpha(\theta)$. In this notation, index α marks the PDF that corresponds to a given value of the regularization parameter α. Although $p_\alpha(\theta)$ may have in general a skew peak, we will assume that a Gaussian distribution centered at θ_0 captures most of the probability mass of the true PDF. Then

$$p_\alpha(\theta) = \frac{1}{\sqrt{\det\,(2\pi C)}} \exp\left[-\frac{1}{2}\ (\theta - \theta_0)\ C^{-1}\ (\theta - \theta_0)^t\right], \tag{22}$$

where C is the error-covariance matrix.

This matrix may be estimated through the matrix of second derivatives of $\mathscr{L}_\alpha(\theta)$ according to its expansion into a Taylor series in the vicinity of the minimum:

$$\mathscr{L}_\alpha(\theta_0 + \Delta\theta) \simeq \mathscr{L}_\alpha(\theta_0) + \frac{1}{2}\,\Delta\theta\,\frac{\partial^2 \mathscr{L}_\alpha(\theta_0)}{\partial\theta^2}\ \Delta\theta^t\,, \tag{23}$$

and

$$C_{ij} = \frac{1}{2}\,\frac{\partial^2 \mathscr{L}_\alpha(\theta_0)}{\partial\theta_i\,\partial\theta_j}\,. \tag{24}$$

If the errors are uncorrelated, equation (22) simplifies to the product of the individual parameter distributions:

$$p_\alpha(\theta) = \frac{1}{\sqrt{\prod_{j=1}^{\nu'}(2\pi\sigma_j^2)}} \exp\left[-\frac{1}{2}\sum_{j=1}^{\nu'}(\theta_j - \theta_{0,j})^2/\sigma_j^2\right], \tag{25}$$

where $\nu' = 2M + 3$ and σ_j are the parameter dispersions.

To estimate exactly the level of $\mathscr{L}_\alpha$ that corresponds to the region containing a certain percentage (say 68% = 1 σ for normal distribution) of the total probability we would need to carry out quite extensive Monte Carlo simulations at each step of our iterative procedure. However, in order to estimate roughly the parameter dispersions we may use instead of $\Delta\mathscr{L}_\alpha = \mathscr{L}_\alpha(\theta_0 + \Delta\theta) - \mathscr{L}_\alpha(\theta_0)$ the corresponding value of $\Delta\chi^2_{\nu'}$, which is computed according to Press et al. (1992). Since the regularization term in $\mathscr{L}_\alpha$ is kept small as compared with the χ^2 term, this estimation of the dispersions is expected not to deviate significantly from the true value. Then the variances in equation (25) can be evaluated as

$$\sigma_j^2 = \frac{\Delta\chi^2_{\nu'}}{\nu}\ C_{jj}^{-1}\,. \tag{26}$$

The definition of the cross-entropy that is the distance between the two distributions p_1 and p_2 (called also the Kullback measure) is given by (see Csiszár 1996; Wu 1997)

$$\mathscr{K}(p_1\,||\,p_2) = \int_{-\infty}^{\infty} p_1(x)\,\log\,[p_1(x)/p_2(x)]\,dx \geq 0\,. \tag{27}$$

It is the nonadditive, nonsymmetric measure being equal to 0 only in case $p_1 = p_2$.

Now suppose that the optimal PDF $p_{\rm opt}(\theta)$ is known. Then to estimate the appropriate α-value we have to minimize the distance between $p_{\rm opt}$ and p_α, i.e., the cross-entropy $\mathscr{K}(p_\alpha\,||\,p_{\rm opt})$. Taking the PDF in form (25), we obtain

$$\mathscr{K}(p_\alpha\,||\,p_{\rm opt}) = \sum_{j=1}^{\nu'} \log\left[\frac{\sigma_j^2(\alpha_{\rm opt})}{\sigma_j^2(\alpha)}\right] + \frac{1}{2}\left[\frac{\sigma_j^2(\alpha)}{\sigma_j^2(\alpha_{\rm opt})} - 1\right] + \frac{[\theta_{0,j}(\alpha) - \theta_{0,j}(\alpha_{\rm opt})]^2}{2\sigma_j^2(\alpha_{\rm opt})}\,. \tag{28}$$

In general we are not given a priori the optimal distribution, but we can construct it adaptively from the sequence of solutions obtained for successive values of α ranging from $\alpha_{\rm min}$ to $\alpha_{\rm max}$ with a step of $\Delta\alpha$. Using the estimation from the previous step as a current approximation for $p_{\rm opt}$, we obtain the following iterative sequence: $\mathscr{K}(p_{\alpha_1}\,||\,p_{\alpha_{\rm min}})$, $\mathscr{K}(p_{\alpha_2}\,||\,p_{\alpha_1})$, ... , $\mathscr{K}(p_{\alpha_{\rm max}}\,||\,p_{\alpha_{\rm max}-\Delta\alpha})$.

Numerical experiments with synthetic spectra have shown that this sequence really converges to 0. The optimum value of $\alpha_{\rm opt}$, i.e., the value for which the recovered T^* was most close to the underlying T used to produce the spectrum, was found to coincide with the point where the

curvature of the trajectory $\mathscr{K}(\alpha_i) \equiv \mathscr{K}(p_{\alpha_i} || p_{\alpha_{i-1}})$ passed through the maximum (see Lucy 1994). Figure 1 illustrates this behavior.

As is known, the curvature of the continuous curve $y(x)$ is

$$\mu = \ddot{y}/(\dot{y}^2 + 1)^{3/2} , \tag{29}$$

where dots indicate differentiation. It is obvious that the value of μ depends on the units in which y and x are measured. Therefore, in order to get uniform results, we always computed μ for the values $\mathscr{K}$ and α normalized to 1, i.e., in the coordinates

$$\hat{\mathscr{K}}, \hat{\alpha} = (\mathscr{K} - \mathscr{K}_{\min})/(\mathscr{K}_{\max} - \mathscr{K}_{\min}),$$
$$(\alpha - \alpha_{\min})/(\alpha_{\max} - \alpha_{\min}) . \tag{30}$$

The derivatives in equation (29) are computed numerically through the common finite differences $\ddot{\mathscr{K}}_i = (\mathscr{K}_{i+1} - 2\mathscr{K}_i + \mathscr{K}_{i-1})/\Delta\alpha^2$ and $\dot{\mathscr{K}}_i = (\mathscr{K}_{i+1} - \mathscr{K}_{i-1})/2\Delta\alpha$. Since numerical differentiation is rather sensitive even to any small uncertainties in the function values, to get the smooth distribution of μ we need to calculate the $\mathscr{K}$ values with very high accuracy. This means that the minimization of $\mathscr{L}$ is to be continued till the stable global minimum with $|\Delta\mathscr{L}/\mathscr{L}| < 10^{-6}$ is achieved. The approximation of $\mathscr{K}(\alpha)$ with smoothing spline can be used as well to obtain the stable numerical derivatives. But it should be noted that if $\mathscr{K}(\alpha)$ is computed with significant errors, then the smoothing spline may noticeably move the maximal curvature point to a wrong value of $\alpha_{\rm opt}$. Thus the only way to derive the reliable estimation of $\alpha_{\rm opt}$ (and hence of T) is to carry out the calculations on each step of the procedure as accurately as possible.

It should be pointed out before going ahead that we can test the estimated value of $\alpha_{\rm opt}$ by using the intrinsic properties of the Kullback measure. As noted above, cross-entropy is the nonsymmetric measure, that is, $\mathscr{K}(p_1 || p_2) \neq \mathscr{K}(p_2 || p_1)$. This property can be used to verify the obtained estimations in the following way: we compute $\mathscr{K}$-values for both upward $\alpha = \alpha_{\min}$ $(\Delta\alpha)$ $\alpha_{\max}$ and downward $\alpha = \alpha_{\max}(-\Delta\alpha)\alpha_{\min}$ sequences and then estimate the corresponding optimal values of α. Their coincidence for both directions may be considered as a simple validity proof. Another useful property is the nonadditivity of the Kullback measure, i.e., $\mathscr{K}(p_{\alpha+\Delta\alpha} || p_\alpha) \neq \mathscr{K}(p_{\alpha+\Delta\alpha/2} || p_\alpha) + \mathscr{K}(p_{\alpha+\Delta\alpha} || p_{\alpha+\Delta\alpha/2})$. This means that if the solution of the inverse problem does exist, then the $\mathscr{K}(\alpha)$-sequences should yield the same $\alpha_{\rm opt}$-value independently of the step size $\Delta\alpha$.

The limiting values of $\alpha_{\min}$ and $\alpha_{\max}$ should be chosen in such a way that the expected goodness-of-fit does not deteriorate strongly ($\chi^2 \lesssim 1$). Although the natural choice of the minimum value seems to be $\alpha_{\min} = 0$, in some cases the α-sequence may be continued into the region of negative α keeping inequality $\mathscr{L}_\alpha > 0$ valid. The extension of the α-sequence below zero becomes an especially essential step when the preliminary calculations reveal a low gradient $\mathscr{K}(\alpha)$-curve over the whole interval $[0, \alpha_{\max}]$, indicating that the maximum curvature point lies outside.

The method described makes it possible to recover the underlying kinetic temperature from spectra of different complexity and quality. It should be mentioned, however, that the procedure yields only a best fit value for parameter(s) without confidence intervals (a pointlike estimation) since the dispersions obtained can be over- or underestimated for the reasons considered above. The actual error limits may be revealed only through numerical experiments with synthetic spectra. The model calculations with noisy data (S/N = 100) and spectral resolutions (FWHM) ranging from 3 km s^{-1} to 12 km s^{-1} have shown, however, that similar unsaturated profiles of C^+, Si^+, and Fe^+ ions provide an accuracy of the kinetic temperature estimation as high as 10%.

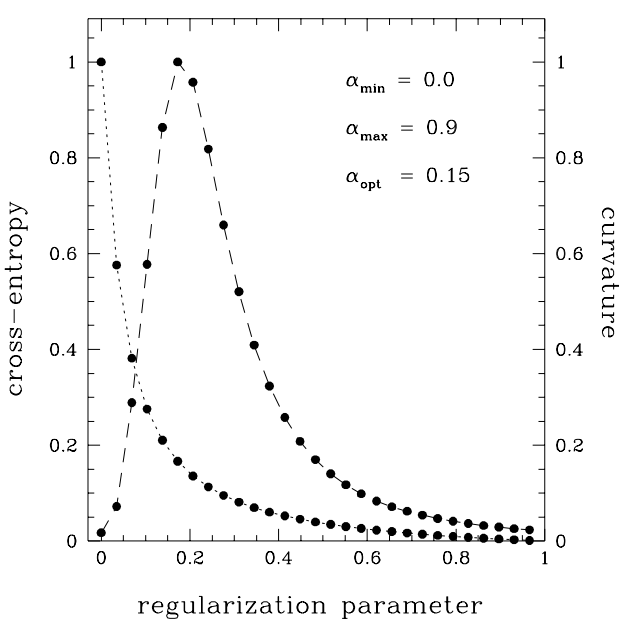

FIG. 1.—Convergence behavior of the cross-entropy defined by equation (28). The filled circles connected by dotted line show the normalized values of $\hat{\mathscr{K}}$ calculated in accord with equation (30). Also plotted is the curvature $\mu/\mu_{\max}$ (*filled circles connected with dashed line*) of the trajectory $\hat{\mathscr{K}}(\hat{\alpha})$. The optimal value of $\alpha_{\rm opt} = 0.15$ corresponds to the maximum curvature at point $\hat{\alpha} = 0.167$. This example is calculated for model 3 from Table 1.

3.2. *Numerical Experiments*

In the previous section we have considered the ERM algorithm. The remaining problem now is to show the accuracy of the ERM solutions and hence their reality.

Since our computational procedure contains several ad hoc assumptions that can hardly be backed with unambiguous mathematical justification, it is natural to prove its validity by recovering the kinetic temperature from the synthetic absorption-line spectra at first. For this purpose, we have generated a variety of line profiles employing different sets of physical parameters and several random realizations of the one-dimensional velocity fields. The calculations were performed for the pairs of lines C II λ1334 + Si II λ1260 and C II λ1334 + Fe II λ2600, which are frequently observed in interstellar and quasar absorption spectra. The procedure may be applied to any other suitable pairs as well.

The physical parameters specifying our cloud model are the column densities of the elements in a pair, the dispersion of the turbulent velocity field σ_t, and the kinetic temperature T. Besides, all synthetic spectra have been convolved with the instrumental profile of different FWHM. In order to make the synthetic spectra look like true observations with an S/R of 100, corresponding Gaussian noise has been added. The model parameters are listed in Table 1.

To calculate synthetic spectra we need to generate stochastic velocity fields at first. Modeling of the stationary random velocity fields $v(s)$ with different correlation ranges

TABLE 1

MODEL PARAMETERS USED TO GENERATE SYNTHETIC SPECTRA OF C II λ1334 , Si II λ1260, C II λ1334, AND Fe II λ2600

Model	Pair	N (cm^{-2})	σ_t (km s^{-1})	T (K)	FWHM (km s^{-1})	l	ε
1.....	C II	4(13)	15	1.5(4)	3	0.1	1.0
	Si II	4(12)					
2.....	C II	4(13)	15	1.5(4)	3	0.1	1.1
	Si II	4(12)					
3.....	C II	4(13)	15	1.5(4)	6	0.1	1.1
	Si II	4(12)					
4.....	C II	4(13)	15	1.5(4)	7	0.25	−0.5
	Si II	4(12)					
5.....	C II	4(13)	15	1.5(4)	7	0.25	0.5
	Si II	4(12)					
6.....	C II	4(13)	15	1.5(4)	7	0.25	−1.5
	Si II	4(12)					
7.....	C II	4(13)	15	1.5(4)	9	0.1	1.0
	Si II	4(12)					
8.....	C II	4(13)	15	1.5(4)	9	0.1	1.1
	Si II	4(12)					
9.....	C II	4(13)	15	1.5(4)	9	0.1	−1.0
	Si II	4(12)					
10.....	C II	4(13)	15	1.5(4)	12	0.1	1.1
	Si II	4(12)					
11.....	C II	4(13)	15	1.5(4)	12	0.1	1.0
	Si II	4(12)					
12.....	C II	4(13)	5	1.5(4)	3	0.5	−1.5
	Si II	4(12)					
13.....	C II	4(13)	5	2.0(3)	3	0.05	−1.5
	Si II	4(12)					
14.....	C II	5.5(13)	20	1.0(4)	3	0.3	−1.5
	Fe II	5.3(12)					
15.....	C II	5.5(13)	20	1.0(4)	6	0.3	−1.5
	Fe II	5.3(12)					

NOTE.—C II λ1334 and Si II λ1260 are represented in models 1–13; C II λ1334 and Fe II λ2600 are represented in models 14 and 15. The parameterized family of velocity correlation functions (31) is defined by the parameters l and ε (see text).

in space is performed through the moving-average method described in the Appendix. To generate the correlated fields, the following parameterized family of correlation functions was chosen (see Elliott et al. 1997):

$$\mathscr{C}_{l,\varepsilon}(s) = \left(1 + \frac{s^2}{l^2}\right)^{\varepsilon/2-1} \cos\left[(2-\varepsilon)\arctan\left(\frac{|s|}{l}\right)\right], \quad (31)$$

where l is a linear scale proportional to the distance over which there is appreciable correlation between the velocity values at two points (see Monin & Yaglom 1975). This family is widely used in the turbulent flow modeling and provides a diversity of scaling behavior as the parameter ε varies in the range $-\infty < \varepsilon < 2$. For instance, regions of negative correlations for the velocity field may be obtained with $\varepsilon < 1$, whereas for $\varepsilon \geq 1$ we have the regime of positive correlations with very long ranges. Parameters l and ε used to generate the velocity fields are listed in Table 1 as well (l is given in units of L).

Listed in Table 1, models 1–11 were constructed to settle the accuracy of the kinetic temperature measurement at different spectral resolutions. The synthetic spectra were calculated for the fixed values of $T = 15{,}000$ K and $\sigma_t = 15$ km s^{-1}, using different velocity fields. The velocity fields were chosen rather at random because our aim was mainly to show the ability of the method to recover the correct temperature from almost any velocity fields. Thereafter the spectra were convolved with Gaussian functions with FWHM = 3, 6, 7, 9, and 12 km s^{-1}. The spectral resolution of 3 km s^{-1} was achieved in the studies of the interstellar absorption lines with *HST*, whereas the intergalactic spectra are being observed at present with the resolutions 6–12 km s^{-1}. The ratio FWHM/$v_{\mathrm{th},2}$ in our model series lies within the range 1–4, meaning that the smoothing effect for FWHM ≥ 6 km s^{-1} becomes very pronounced.

To apply our ERM procedure to another kind of absorption spectra, we have calculated the synthetic spectra for $\sigma_t = 5$ km s^{-1} and the temperatures $T = 15{,}000$ K and 2000 K (models 12 and 13, respectively). The last two models, 14 and 15, were constructed to test the procedure for different ratios of m_1/m_2 and $\sigma_t/v_{\mathrm{th},2}$.

Table 2 lists the recovered kinetic temperatures T^* along with some other estimated parameters. Comparison of columns (7) and (8) shows the high efficiency of the proposed computational procedure, which allows us to estimate T with an accuracy of $|\Delta T/T| \lesssim 10\%$ even for the rather smeared out spectra (models 7–11).

In column (6) of Table 2 we list the values of $\zeta = \beta_2/\beta_1$. Numerical experiments have shown that for $\zeta \gtrsim 0.9$ the dispersion of T^*, σ_{T^*}, calculated through equation (26), changes its behavior and begins to increase with increasing regularization parameter α. Such a peculiar pattern of σ_{T^*} stems from the fact that at $\zeta \gtrsim 0.9$, the off-diagonal elements

TABLE 2

MODEL PARAMETERS DERIVED FROM THE SYNTHETIC SPECTRA THROUGH THE EQUI-DISPERSION DECONVOLUTION (. [12]) WITH THE SUBSEQUENT ENTROPY-REGULARIZED MINIMIZATION OF THE OBJECTIVE FUNCTION (eq. [20])

Model	α_{min}	α_{opt}	M	χ^2	ζ	T^*[a], K	T, K
1.....	0.0	0.2	8	0.713	0.86	14271	15000
2.....	−0.4	0.0	7	0.674	0.77	15097	15000
3.....	0.0	0.15	4	0.725	0.89[b]	13775	15000
4.....	−0.15	0.0	4	0.364	0.84	14576	15000
5.....	0.0	0.275	4	0.797	0.85	15401	15000
6.....	0.0	0.2	5	0.814	0.86	15866	15000
7.....	−0.037	−0.032	4	0.710	0.93[b]	14530	15000
8.....	−0.069	−0.062	4	0.409	0.89	13537	15000
9.....	0.0	0.012	4	0.741	0.95[b]	13910	15000
10.....	−0.006	−0.003	2	0.408	0.96[b]	14473	15000
11.....	−0.0203	−0.0198	4	0.458	0.93[b]	14632	15000
12.....	−0.2	0.5	2	0.257	0.71	16112	15000
13.....	0.0	0.02	5	0.752	0.92[b]	1816	2000
14.....	0.0	0.3	11	0.763	0.75	10461	10000
15.....	−0.04	0.02	8	0.756	0.85	10081	10000

[a] T^*: estimated temperature; T: adopted temperature.
[b] Increasing dispersion σ_{T^*} (see text for details).

of the error-covariance matrix C in equation (22) are already not small as compared with C_{ii} and, hence, the approximation (25) becomes rather vague since the errors become strongly correlated. However, the iterative procedure continues to deliver an acceptable T estimation. The procedure fails when $\zeta \approx 1$. This is the case when the ratio FWHM/$v_{th,2}$ is large and the intensity fluctuations within the line profiles are considerably smoothed, which in turn makes the widths of the subcomponents practically indistinguishable.

The consequent steps of our computational scheme are illustrated in Figures 2–4. The case of positive correlations

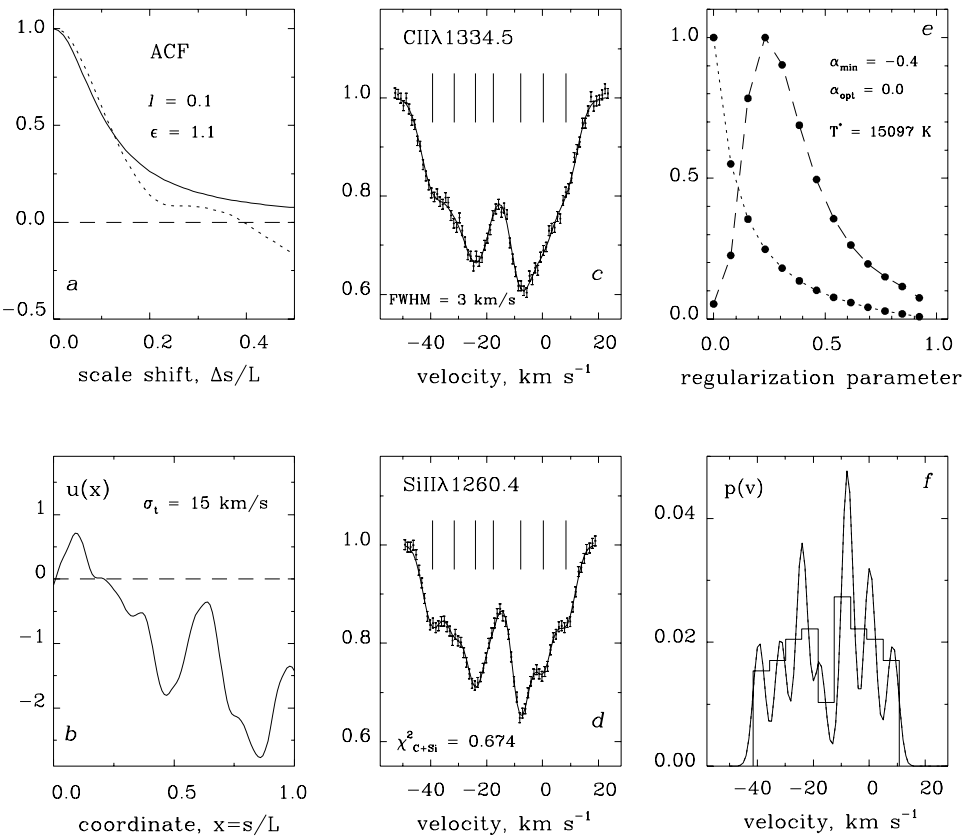

FIG. 2.—(*a*) Autocorrelation functions: the solid curve shows the adopted model; the dotted curve is calculated from the random realization of the velocity field shown in (*b*). (*c*, *d*) Velocity plots of the simulated spectra (*dots and 1 σ error bars*) and the calculated profiles convolved with the instrumental resolution of FWHM = 3 km s^{-1} (*solid curves*), corresponding to model 2 in Table 1. (*e*) Cross-entropy as function of the normalized regularization parameter $\hat{\alpha}$ (*filled circles connected by dotted line*) and the curvature of its trajectory (*filled circles connected by dashed line*). (*f*) Simulated one-dimensional velocity distribution (*histogram*) and its estimation through the C II (or Si II) profiles. See text for more details.

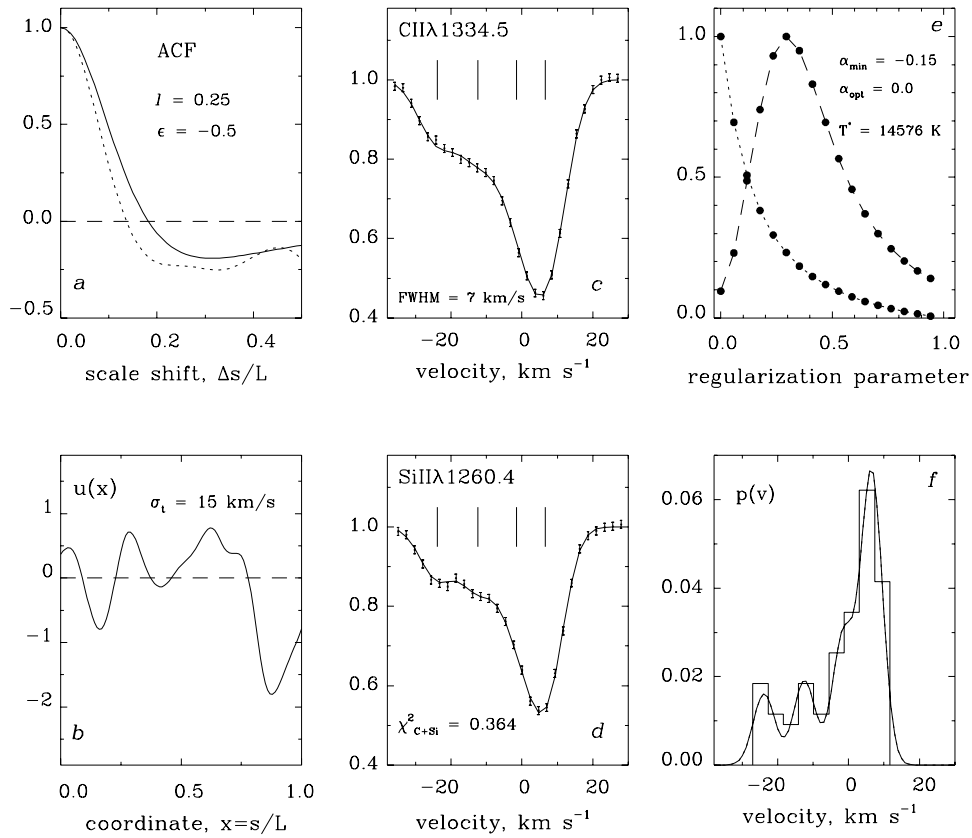

FIG. 3.—Same as Fig. 2, but for a different velocity field and FWHM = 7 km s^{-1} (model 4 in Table 1)

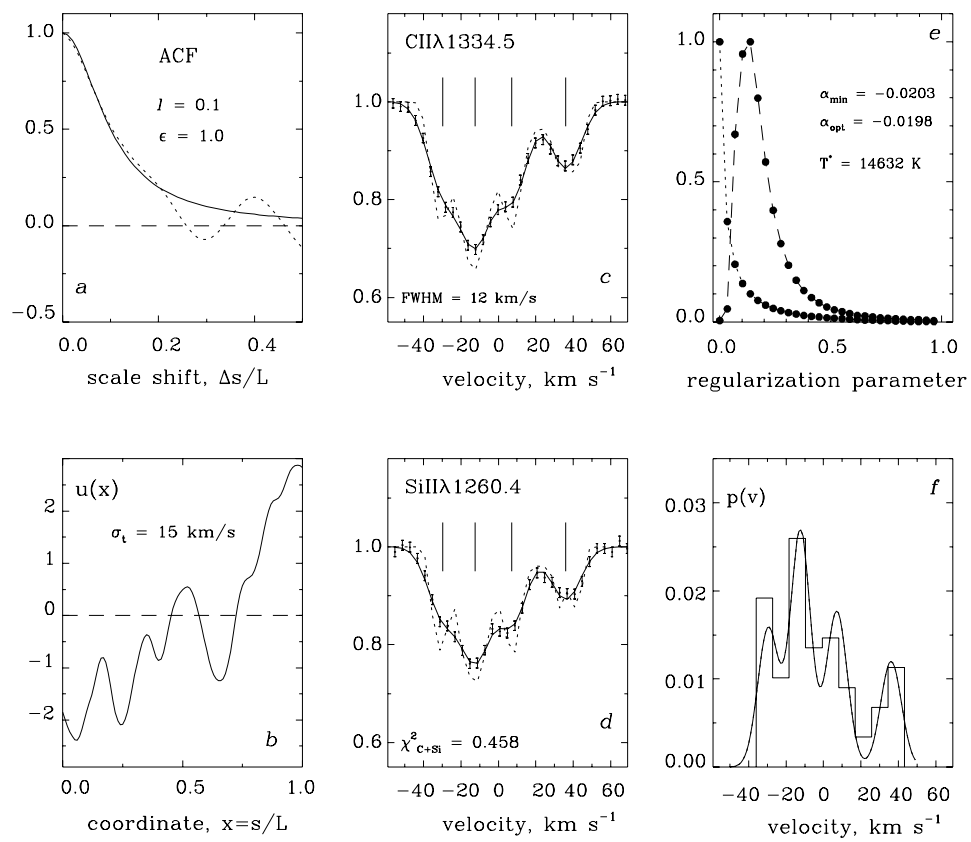

FIG. 4.—Same as Fig. 2, but for a different velocity field and FWHM = 12 km s^{-1} (model 11 in Table 1). The original (unconvolved) spectra are shown in (*c*) and (*d*) by dotted curves as well. Note the doublet-like structure at $\Delta v = 40$ km s^{-1} in the Si II spectrum, which is completely smeared out after convolution.

for the large-scale velocity field ($\varepsilon = 1.1$ and 1.0) is presented in Figures 2 and 4, respectively. Figure 2*a* shows the adopted correlation function $\mathscr{C}_{l,\epsilon}$ with a solid line and the autocorrelation function (ACF) calculated for the random realization of $v(s)$ with a dotted line. The computed ACF may deviate from the exact correlation function because of the finite thickness of the absorbing region. Figure 2*b* shows the corresponding velocity field $u(x) = v(x)/\sigma_t$, where $x = s/L$. This field leads in turn to the complex profiles of C II and Si II. Both profiles are convolved with a Gaussian function having the width of 3 km s^{-1} (FWHM), and then a Gaussian noise of S/N = 100 has been added. The final patterns are shown in Figures 2*c* and 2*d* by dots with corresponding error bars. The C II and Si II lines were fitted simultaneously employing equations (12), (19), and (20). The fit was performed with the increasing number of modes M until a χ^2-value of $\lesssim 1$ was achieved. In Figures 2*c* and 2*d* the best-fitting profiles with $M = 7$ equidispersion components (located at the velocities shown by the tick marks) are plotted as solid curves superimposed on the simulated data. The joint χ^2-value per degree of freedom ($\nu = 129$) is indicated at the bottom of Figure 2*d*. Figure 2*e* illustrates that if a feasible MaxEnt solution does exist, then the Kullback measure $\hat{\mathscr{K}}(\hat{\alpha})$ calculated through equations (28) and (30) converges with increasing $\hat{\alpha}$. The optimal value of $\alpha = 0.0$ corresponding to the maximum curvature of the trajectory $\hat{\mathscr{K}}(\hat{\alpha})$ leads to the estimation $T^* = 15{,}097$ K. Given the kinetic temperature, we may calculate the radial velocity distribution function $\phi_t(v)$ using equation (18) and either the C II or Si II spectrum. For both sets of data the solution is expected to be identical. The results obtained are shown in Figure 2*f* by solid curves. The histogram plotted in Figure 2*f* is the underlying distribution function $p(v)$, which corresponds to the velocity profile $v(x) = \sigma_t u(x)$ shown in Figure 2*b*. Since all curves are very much alike, we consider this result as an additional justification of our procedure.

The regime of negative correlations ($\varepsilon = -0.5$) for the random velocity field is illustrated in Figure 3 (here FWHM = 7 km s^{-1}). The case for the lowest resolution of 12 km s^{-1} is demonstrated in Figure 4. The fitting parameters for these examples are listed in Table 2. Analyzing all results, we may conclude that the procedure yields stable estimations of T and $\phi_t(v)$ for the whole range of spectral resolutions considered.

4. DISCUSSION

4.1. *Comparison with the Standard Voigt Deconvolution*

Based on the Voigt fitting, most previous approaches extracted information on the gas kinetic temperature from the values of b found for the various subcomponents of the complex profiles. As a result, absorbing regions have usually been characterized by a variety of T values that, in some cases, ranges from ≈ 0 K up to $\approx 10{,}000$ K (e.g., Spitzer & Fitzpatrick 1995). It seems quite natural to apply the standard Voigt fitting procedure to our synthetic spectra to compare its result with the estimation obtained by the proposed method.

To carry out such analysis, we generated the C II λ1334 and Fe II λ2600 absorption profiles (Fig. 5, model 14 from Table 1) convolved with the instrumental function of FWHM = 3 km s^{-1}. The corresponding Gaussian noise with an S/R of 100 was added as well. Then we considered the spectra shown in Figure 5 as "observational" data and tried to analyze them in the standard manner, i.e., to fit them with Voigt profiles until a satisfactory result with $\chi^2 \lesssim 1$ was achieved. A simultaneous fit to the 10 subcomponents gave the reduced χ^2 per degree of freedom of 0.687 ($\nu = 172$).

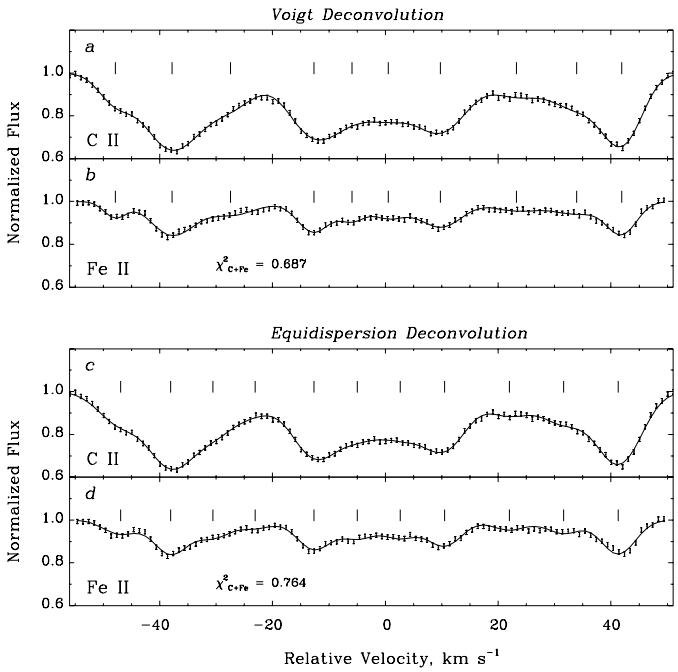

FIG. 5.—(*a*, *b*) Velocity plots of the C II λ1334 and Fe II λ2600 synthetic spectra (*dots with 1 σ error bars*; model 14 in Table 1). The smooth curves show the Voigt profiles convolved with the instrumental resolution of 3 km s^{-1} (FWHM), which produce the best simultaneous fit to all data. The velocity positions for each of 10 absorption components are labeled by the tick marks at the top of each panel. (*c*, *d*) Same as (*a*, *b*), but for the ERM result based on the equidispersion deconvolution of the C II and Fe II profiles with a single kinetic temperature (see text for more details).

The parameter estimates are listed in Table 3, along with the corresponding values of the gas temperatures T_i^* and the turbulent velocities σ_i^* for the "individual cloudlets." The revealed values clearly demonstrate a wide spread of the apparent b-parameters resulting in the large variations of T: from ≈ 10 K to $\approx 18{,}000$ K, whereas the spectra have been produced by using a single underlying temperature $T = 10{,}000$ K. Moreover, taken at face value, the relative widths of b_i(C II) and b_i(Fe II) lead to unlikely small values of $\sigma_i^* \approx 1 - 4$ km s^{-1}, i.e., to a significantly lower turbulent velocity than adopted $\sigma_t = 20$ km s^{-1}.

The same synthetic spectra, having been treated by the proposed procedure, yield a single value for the gas temperature of 10,461 K (see Table 2). The corresponding equidispersion deconvolution (with $M = 11$ components) is plotted in panels *c* and *d* in Figure 5.

These results lead to the conclusion that the spread of the gas temperature found in some regions of the ISM and in the extragalactic intervening clouds may be unphysical and stems purely from an inappropriate method of data analysis.

4.2. *The* C II *and* Si II *Profiles Observed in QSO 1937−1009*

We turn now to a brief discussion of the application of the present computational technique to recover the kinetic temperature from observational data. For this purpose we have chosen the high-quality Keck spectra of the quasar Q1937−1009 (Tytler, Fan, & Burles 1996) showing metal absorption lines at the redshift $z = 3.572$. Since this system is the only one where the deuterium absorption was observed at high redshift in both the D Lyα and Lyβ lines, it has been thoroughly studied using different methods (Tytler & Burles 1997; Levshakov et al. 1998; Burles & Tytler 1998).

According to Tytler & Burles, all metal absorption lines seen at this redshift (C II, C IV, Si II, Si IV) "appear to have the same profiles." This may lead to the suggestion that these metals are similarly distributed in the velocity space and hence a single gas temperature could be sufficient to describe their profiles. To estimate its value, we have selected the C II λ1334 and Si II λ1260 lines observed with FWHM = 8 km s^{-1} and S/N = 56 and 100, respectively. The original normalized data are shown in Figure 6 by dots with the corresponding error bars.

The Voigt fitting analysis previously performed by Tytler et al. (1996) revealed two gas clouds separated by 15 km s^{-1} (the blue and the red components). The physical parameters found for these components are (Tytler & Burles) $T_{\rm blue} = 17{,}100 \pm 1300$ K, $\sigma_{\rm blue} = 3.35 \pm 0.56$ km s^{-1}, $T_{\rm red} = 19{,}000 \pm 5800$ K, $\sigma_{\rm red} = 6.75 \pm 0.28$ km s^{-1} (where $\sigma \equiv b_{\rm turb}/\sqrt{2}$).

This system has also been analyzed by another method based on the mesoturbulent concept (Levshakov et al. 1998). In this study the H+D Lyα, Lyβ and higher order Lyman series absorption lines (up to Ly-19) have been treated using the reverse Monte Carlo (RMC) procedure (computational details are given in Levshakov et al. 1998, 1999). The gas temperature, T^*, and the ensemble turbulent velocity dispersion, $\tilde{\sigma}_t^*$, estimated within the framework of the one-cloud model were found to lie in the ranges from 10,900 to 14,300 K and from 18.5 to 22.3 km s^{-1}, respectively.

Applying the present procedure to the C II and Si II lines, we obtained the gas temperature $T^* = 14{,}090$ K. Table 4 and Figure 6 illustrate our results. The best-fitting profiles with $M = 5$ equidispersion components are shown in panels *a* and *b* by solid lines with the tick marks indicating the velocity positions for the separate components. Figure 6*c* demonstrates the radial velocity distribution function (*solid curve*) calculated through equation (18). The square root of the central second moment of this distribution $\sigma_t^* = 8.6$ km s^{-1} depicted in panel *c* may be considered as a measure of the one-dimensional velocity scatter along the space coordinate. This quantity naturally falls below the ensemble velocity dispersion $\tilde{\sigma}_t^*$ because the sample of the velocity components parallel to the line of sight is not complete in the statistical sense (see Levshakov & Kegel 1997 for details). Also shown in Figure 6*c* is a histogram that represents the velocity distribution derived from the analysis of the hydrogen and deuterium lines by the RMC procedure.

In general we would expect H I and metals to give similar temperatures. They would be identical if absorbing gas was fully homogeneous. Analyzing our results on the $z = 3.572$

TABLE 3

THE STANDARD VOIGT FITTING PROCEDURE RESULTS

Number	Δv (km s^{-1})	b_i(C II) (km s^{-1})	b_i(Fe II) (km s^{-1})	T_i^* (K)	σ_i^* (km s^{-1})
1	−47.86	3.75	2.09	8896	0.9
2	−37.79	6.46	4.90	16212	3.1
3	−27.42	5.998	5.997	11	4.2
4	−12.68	5.79	3.64	18590	2.0
5	−5.90	5.06	2.50	17821	0.7
6	0.52	5.20	3.76	11854	2.3
7	9.78	6.07	4.90	11837	3.2
8	23.24	6.00	5.37	6564	3.7
9	33.93	5.86	5.63	2467	3.9
10	41.90	4.38	3.18	8310	1.9

NOTE.—Model parameters evaluated simultaneously from the C II λ1334 and Fe II λ2600 synthetic spectra (Fig. 5) by fitting 10 individual subcomponents numbered in the order of increasing relative velocity Δv. Reduced χ^2 (with 172 degrees of freedom) is equal to 0.687. The adopted values for the kinetic temperature, T, and the rms turbulent velocity dispersion, σ_t, are, respectively, equal to 10^4 K and 20 km s^{-1} (model 14 in Table 1).

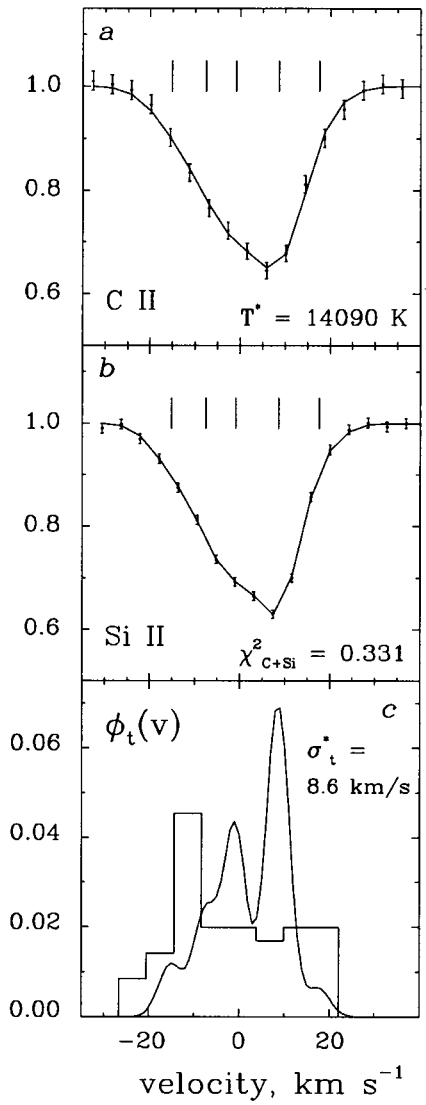

FIG. 6.—(*a*, *b*) Normalized data points with 1 σ error bars for HIRES echelle spectrograph observations (FWHM = 8 km s^{-1}) on the Keck telescope of the C II λ1334 and Si II λ1260 absorption features (the signal-to-noise per pixel is, respectively, 56 and 100) at the redshift $z = 3.572$ toward the quasar 1937−1009 (Tytler & Burles 1997). The ERM result (reduced $\chi^2 = 0.331$ with 24 degrees of freedom) for C II and Si II (*solid lines*) is based on simultaneously fitting the multiple equidispersion lines located at the velocities shown by the tick marks at the top of each panel. The evaluated kinetic temperature $T^* = 14090$ K is plotted in (*a*). (*c*) The radial velocity distribution function $\phi_t(v)$ restored through the observed profile of the C II (or Si II) line using eq. (18) and the model parameters from Table 4. The square root of the central second moment σ_t^* of the $\phi_t(v)$ distribution is also shown in the panel. For comparison, the histogram reproduces the velocity distribution function estimated by the reverse Monte Carlo (RMC) procedure (Levshakov et al. 1998a) through the analysis of the H+D Lyα, Lyβ, and the higher order Lyman series lines (up to Ly-19) from the same absorption-line system.

system we may conclude that both RMC and ERM methods give the consistent estimate of the kinetic temperature, $T^* \simeq 14{,}000$ K. As for the velocity distribution of neutral hydrogen and deuterium and the velocity distribution of ionized metals, they apparently differ (see Fig. 6*c*). This difference, however, stems from the observed asymmetry of the deuterium and the optically thin metal absorption lines (Tytler & Burles): the former exhibits the blue-side asymmetry, whereas the latter show the red-side skewness. The interpretation of this result may be as

TABLE 4

THE FIT BASED ON THE ENTROPY-REGULARIZED MINIMIZATION

Number	v_j (km s^{-1})	a_j(C II)	a_j (Si II)
1.....	−15.18	0.813	0.833
2.....	−7.56	1.619	1.658
3.....	−0.93	2.998	3.071
4.....	8.57	4.930	5.051
5.....	17.62	0.445	0.456

NOTE.—Model parameters evaluated simultaneously from the observed C II λ1334 and Si II λ1260 spectra (Fig. 6) by fitting five equidispersion components numbered in the order of increasing velocity position v_j. Reduced χ^2 (with 24 degrees of freedom) is equal to 0.331. The estimated value for the kinetic temperature is $T^* = 14{,}090$ K, and the widths of the components are equal to β^*(C II) = 5.735 km s^{-1} and β^*(Si II) = 4.671 km s^{-1} (see eq. [12]).

follows. It is generally believed that most metal absorption-line systems observed in QSO spectra arise in the far outer parts of intervening galaxies or in the intergalactic medium where the main source of ionization is photoionization due to the background UV-flux. If the temperature of about 14,000 K is the mean value for the absorbing gas at $z = 3.572$, which is in thermal equilibrium, then variations in the fractional ionization of different species along the line of sight are mainly governed by the density fluctuations $n_{\rm gas}$ within this region because the thermal and ionization state of the gas is described by the ionization parameter U, which is the ratio of the density of ionizing photons to the total gas density. Ionization models of optically thin in the Lyman continuum intergalactic gas at constant pressure, photoionized by QSOs, show that the equilibrium temperature is weakly dependent on U for metallicities below solar and $-4.7 < \log U < -1.8$, where $T \propto U^{1/8}$ (Donahue & Shull 1991). The deviations between the apparent radial velocity distribution functions may occur when the fractional ionization of different elements responds in different ways to the changes in U. Such deviations may be utilized to place constraints on the density fluctuations within the absorbing gas. This problem will be studied in detail elsewhere.

5. CONCLUSIONS

The outcome of our study, aiming to provide a measurement of the gas kinetic temperature from *similar* complex absorption-line spectra of ions with different atomic weights, is as follows.

1. A new method is developed for using interstellar and intergalactic absorption-line spectra to investigate the intervening gas temperature. It is based on the assumption that a pair of elements has the same temperature and bulk motion within the absorbing region, resulting in similar observed spectra. The method utilizes the Fourier transform of the observed profiles with the subsequent entropy-regularized minimization of the χ^2 function augmented by a penalty function to gain a stable solution of the inverse problem of spectral analysis (the ERM method)

2. The computational procedure has been tested on a variety of synthetic spectra generated in stochastic velocity fields with different correlation scales. The procedure

proved to be very effective and robust, allowing us to recover the temperature with high accuracy, $|\Delta T/T| \lesssim 10\%$, in the range of spectral resolutions from 3 km s^{-1} to 12 km s^{-1} (FWHM).

3. The application of the standard Voigt fitting analysis to the synthetic spectra calculated in the framework of the homogeneous temperature model with $T = 10^4$ K revealed a wide scatter of the gas temperature among the individual "cloudlets"—from 10 K to 1.8×10^4 K. This result demonstrates that the scattering of T reported in the literature may have a nonphysical nature and may be caused by an inappropriate methodology.

4. The asymmetric C II λ1334 and Si II λ1260 lines observed with the Keck I telescope at the redshift $z = 3.572$ toward quasar 1937−1009 by Tytler et al. (1996) have been treated by the proposed method in order to evaluate the underlying gas temperature. The obtained estimation of $T = 14{,}090$ K lies in the range consistent with the previously derived values of T from the analysis of the H + D Lyα and Lyβ and higher order Lyman series profiles by the reverse Monte Carlo method (Levshakov et al. 1998).

It should be emphasized once again that the proposed method can be applied only to similar spectra. In reality, different (nonsimilar) profiles are observed as well (see, e.g., Huang et al. 1995; Songaila 1998). These may be caused by a variety of physical reasons—the overlapping of cold and hot gas clouds due to the Doppler shifts of their radial velocities, variations in the ionizing flux produced by local sources and/or collisional ionizations in higher density subregions, both leading to the diversity in the ionization fractions for different elements, etc.—and hence there cannot be a single physical model to treat such observational data.

The authors are grateful to David Tytler for sharing his calibrated Keck I/HIRES echelle spectra of Q1937−1009 and for a careful reading the manuscript. We also thank Wilhelm Kegel for his valuable comments and suggestions, which have helped us much in this study. S. A. L. gratefully acknowledges the hospitality of the Osaka University and the National Astronomical Observatory of Japan, where this work was performed.

APPENDIX

THE MOVING-AVERAGE METHOD FOR SIMULATING GAUSSIAN RANDOM FIELDS

Gaussian random fields arise in a wide variety of astrophysical problems, including gas flows, large-scale motions, turbulence, etc. To study these problems one needs to model the stochastic fields with given characteristics (power spectrum or covariance function). The moving-average method employed in our modeling of the intervening velocity fields is able to reproduce the true covariances over larger scales than the most common spectral (Fourier) approximation (Pen 1997; Elliott et al. 1997). The description below in general follows that presented in Elliott et al.

Consider the Gaussian random field $v(s)$ with the covariance function $R(s)$ and the power spectrum $S(k)$. $R(s)$ and $S(k)$ are related through common equations representing the direct and inverse Fourier transforms correspondingly:

$$S(k) = \int_{-\infty}^{+\infty} R(s) e^{2\pi i k s}\, ds\ , \tag{A1}$$

and

$$R(s) = \int_{-\infty}^{+\infty} S(k) e^{-2\pi i k s}\, dk\ . \tag{A2}$$

Define now the function $G(s)$, which is the Fourier transform of the square root of the power spectrum $S(k)$:

$$G(s) = \int_{-\infty}^{+\infty} S^{1/2}(k) e^{2\pi i k s}\, dk\ . \tag{A3}$$

Then $v(s)$ can be represented in the form

$$v(s) = \int_{-\infty}^{+\infty} G(s' - s)\, d\mathrm{W}(s')\ , \tag{A4}$$

where $\mathrm{W}(s)$ is the Wiener process with unit variance (see, e.g., Cox & Miller 1965).

The moving-average method stems from the discretization of (A4), resulting in the approximation

$$\hat{v}(s) = \sum_{i=-p}^{p} G(r_i - s)\, Z(r_i)\ , \tag{A5}$$

where Z is a Gaussian random variable with mean zero and variance $\langle Z^2 \rangle = \Delta r$, and Δr is the step of the equally spaced grid points.

Gaussian fields are considered to be equal if they have the same mean and covariance function. Therefore, to test whether the approximation (A5) represents the real field, we have to compare the covariance function of the approximated field with that which was adopted. In this way we may estimate the appropriate step size Δr and the number of the grid points p. The proper values of Δr and p should provide minimal difference between the calculated and adopted covariance functions.

REFERENCES

Burles, S., & Tytler, D. 1998, ApJ, 499, 699
Cox, D. R., & Miller, H. D. 1965, The Theory of Stochastic Processes (London: Chapman & Hall)
Csiszár, I. 1996, in Maximum Entropy and Bayesian Methods, eds. K. M. Hanson & R. N. Silver (Dordrecht: Kluwer), 35
Donahue, M., & Shull, J. M. 1991, ApJ, 383, 511
Elliott, F. W., Jr, Horntrop, D. J., & Majda A. J. 1997, Chaos, 7, 39
Fitzpatrick, E. L., & Spitzer, L., Jr. 1997, ApJ, 475, 623
Huang, J.-S., Songaila, A., Cowie, L. L., & Jenkins, E. B. 1995, ApJ, 450, 163
Levshakov, S. A., & Kegel, W. H. 1997, MNRAS, 288, 787
Levshakov, S. A., Kegel, W. H., & Takahara, F. 1998, ApJ, 499, L1
———. 1999, MNRAS, 302, 707
Lu, L., Sargent, W. L. W., Barlow, T. A., Churchill, C. W., & Vogt, S. 1996, ApJS, 107, 475
Lucy, L. B. 1994, A&A, 289, 983
Monin, A. S., & Yaglom, A. M. 1975, Statistical Fluid Mechanics: Mechanics of Turbulence, Vol. 2, (Cambridge: MIT)
Pen, U.-L. 1997, ApJ, 490, L27
Press, W. H., Teukolsky, S. A., Vetterling, W. T., & Flannery, B. P. 1992, Numerical Recipes in C (Cambridge: Cambridge Univ. Press)
Prochaska, J. X., & Wolfe, A. M. 1997, ApJ, 487, 73
Songaila, A. 1998, AJ, 115, 2184
Spitzer, L., Jr. 1978, Physical Processes in the Interstellar Medium (New York: Wiley)
Spitzer, L., Jr, & Fitzpatrick, E. L. 1993, ApJ, 409, 299
———. 1995, ApJ, 445, 196
Shu, F. H. 1992, Gas Dynamics (Sausalito: University Science Books)
Tikhonov, A. N., & Arsenin, V. A. 1977, Solutions of Ill-Posed Problems (Washington, DC: Winston & Sons)
Traving, G. 1975, in Problems in Stellar Atmospheres and Envelopes, eds. B. Baschek, W. H. Kegel, & G. Traving (Berlin: Springer), 325
Tripp, T. M., Lu, L., & Savage, B. D. 1997, ApJS, 112, 1
Tytler, D., & Burles, S. 1997, in Origin of Matter and Evolution of Galaxies, ed. T. Kajino, Y. Yoshii, & S. Kubono (Singapore: World Science), 37
Tytler, D., Fan, X.-M., & Burles, S. 1996, Nature, 381, 207
Wu, N. 1997, The Maximum Entropy Method (Heidelberg: Springer)